# ADVANCED FUNCTIONAL MATERIALS

## Supporting Information

# From Groundwork to Efficient Solar Cells: On the Importance of the Substrate Material in Co-Evaporated Perovskite Solar Cells

*Tobias Abzieher,\* Thomas Feeney, Fabian Schackmar, Yidenekachew J. Donie, Ihteaz M. Hossain, Jonas A. Schwenzer, Tim Hellmann, Thomas Mayer, Michael Powalla, and Ulrich W. Paetzold\**

# Supporting Information

**From Groundwork to Efficient Solar Cells: On the Importance of the Substrate Material in Co-Evaporated Perovskite Solar Cells**

*Tobias Abzieher, Thomas Feeney, Fabian Schackmar, Yidenekachew J. Donie, Ihteaz M. Hossain, Jonas A. Schwenzer, Tim Hellmann, Thomas Mayer, Michael Powalla, and Ulrich W. Paetzold*
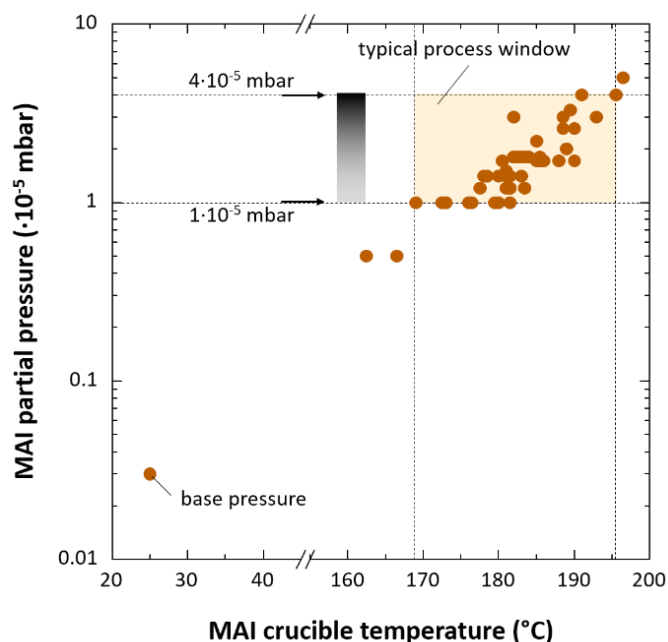


**Fig. S1.** Relation between MAI source temperature and MAI partial pressure in the evaporation system employed in this work. Within the relevant process window, enabling the fabrication of efficient perovskite absorbers, the MAI partial pressure is two orders of magnitude larger than the base pressure of $< 5 \times 10^{-7}$ mbar. Data points were taken from several independent co-evaporation runs.
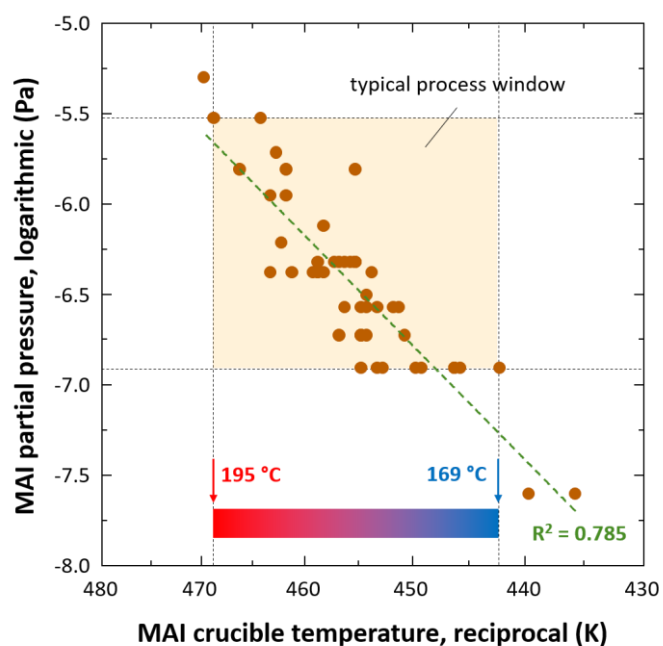
**Fig. S2.** Estimation of the (temperature constant) enthalpy of evaporation of MAI. Logarithmic plot of the MAI partial pressure values from Figure S1 according to the Clausius-Clapeyron relation. The enthalpy of evaporation of MAI $\Delta H_0$ is calculated from the slope of the linear regression to be $\Delta H_0 = (104.8 \pm 7.8)\text{kJ} \cdot \text{mol}^{-1}$. The comparatively small value explains the strong increase in MAI partial pressure during co-evaporation of MAI and $PbI_2$.
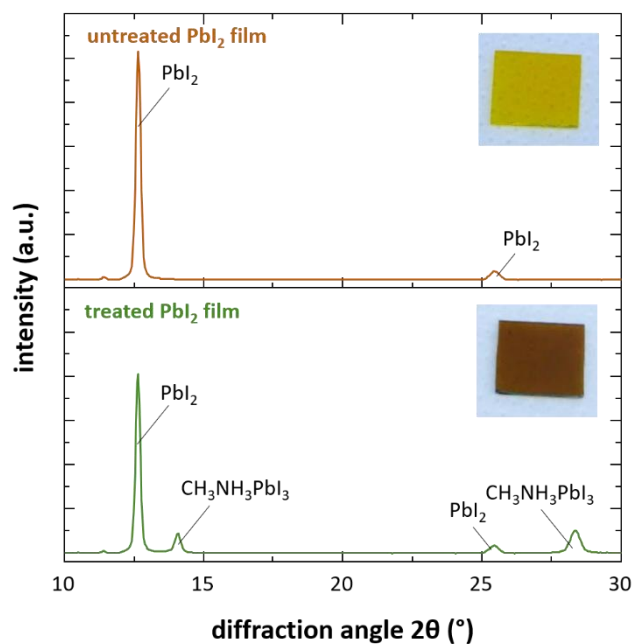
**Fig. S3.** Proof of chemical-vapor-deposition-like reaction paths between $PbI_2$ and MAI during co-evaporation. A pre-deposited dense $PbI_2$ thin film with a thickness of about 250 nm is placed inside the evaporation system and brought into contact with the typical MAI background atmosphere present during the co-evaporation. In order to prevent any effusive flux of MAI reaching the $PbI_2$ thin film, the shutter is kept closed during the entire process. Based on the X-ray diffraction (XRD) pattern of the treated thin film, partial conversion into perovskite without an effusive flux reaching the substrate is clearly visible. This is expected to be a relevant reaction path during the comparatively slow co-evaporation process employed in this work. The insets show photographs of the respective layers illustrating the conversion of $PbI_2$ into perovskite.
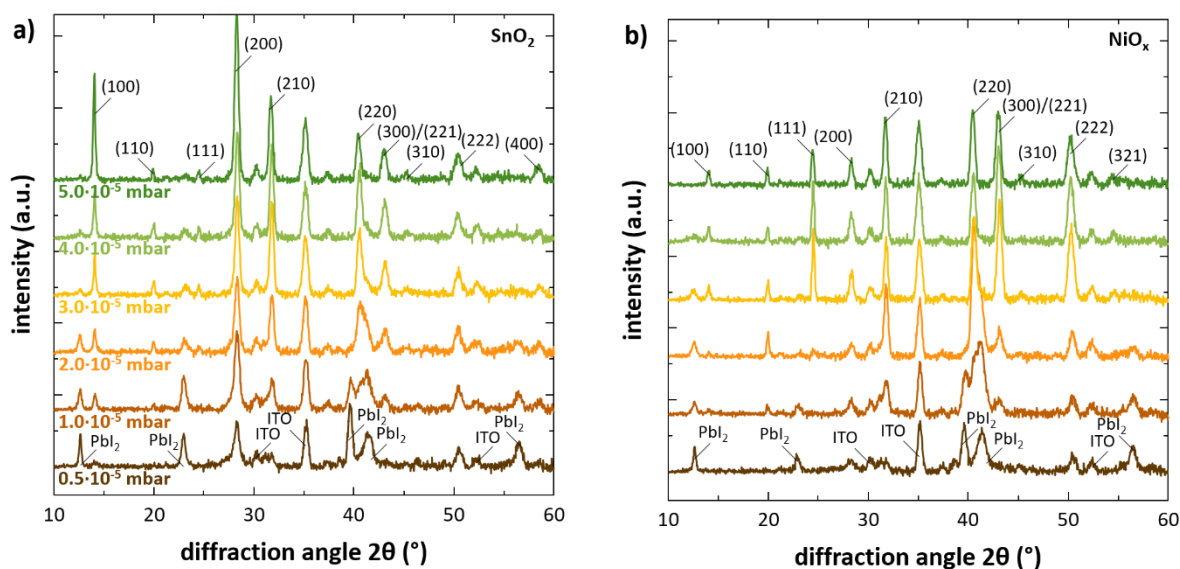
3

**Fig. S4.** X-ray diffraction (XRD) investigations of perovskite thin films grown on top of (a) $SnO_2$ and (b) $NiO_x$ substrates at different MAI partial pressures. As for $TiO_2$ and PTAA, a continuous increase in the conversion of $PbI_2$ into perovskite with increasing MAI partial pressure is apparent. Similar to perovskite thin films grown on $TiO_2$, a preferred orientation of the thin films along the {100} crystal planes is observed for thin films grown on $SnO_2$, while thin films grown on $NiO_x$ show a preferred orientation along {110} and {111} crystal planes similar to thin films grown on PTAA.
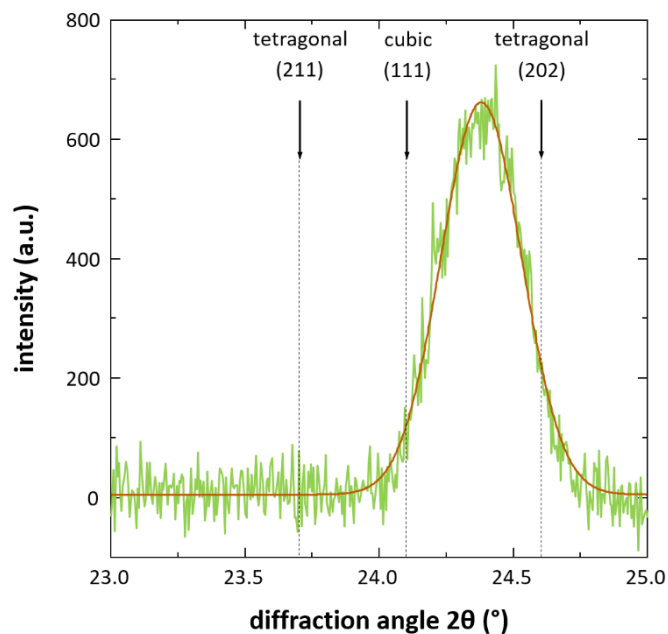
**Fig. S5.** High resolution X-ray diffractogram of the cubic (111) diffraction peak of a co-evaporated perovskite thin film. The characteristic peak splitting of the cubic (111) peak into the (211) and (202) peak, which would be expected for a tetragonal $CH_3NH_3PbI_3$ thin film at room temperature, cannot be observed in the co-evaporated thin films employed in this study, indicating a freezing of the cubic structure during co-evaporation.
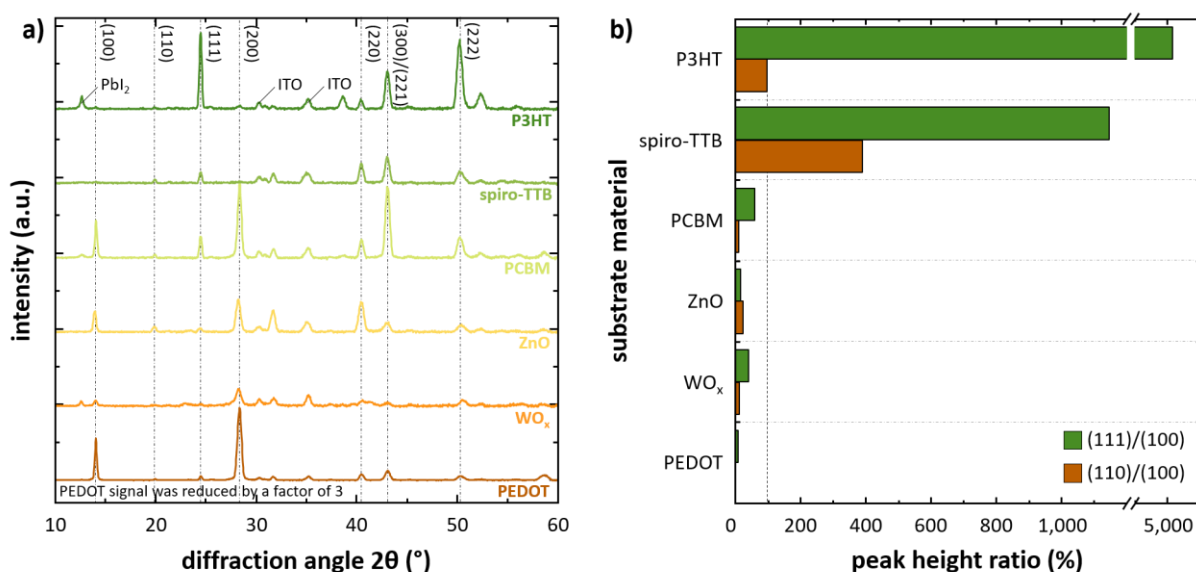
**Fig. S6.** X-ray diffraction (XRD) investigations on perovskite absorbers grown on top of additional substrate materials supplementary to those highlighted in the main manuscript. (a) X-ray diffractograms for absorbers grown on top of PEDOT:PSS, $WO_x$, ZnO, PCBM, spiro-TTB, and P3HT. (b) Ratio of the peak heights for the {100},{110}, and {111} crystal planes for absorbers grown on different substrate materials. Similar to the highlighted substrate materials in the main manuscript, different preferred crystal orientations and in turn growth directions are observed, with P3HT, spiro-TTB, and PCBM following the behavior of PTAA and $NiO_x$, while ZnO, $WO_x$, and PEDOT:PSS are better described by the crystallographic properties of $TiO_2$ and $SnO_2$. Similar to the case of absorbers grown on top of $TiO_2$, a delayed conversion of $PbI_2$ into perovskite is apparent for absorbers grown on $WO_x$ – both visually and based on the weak and wide perovskite diffraction peaks. Due to the very strong signal, the diffractogram of PEDOT:PSS has been reduced by a factor of 3.
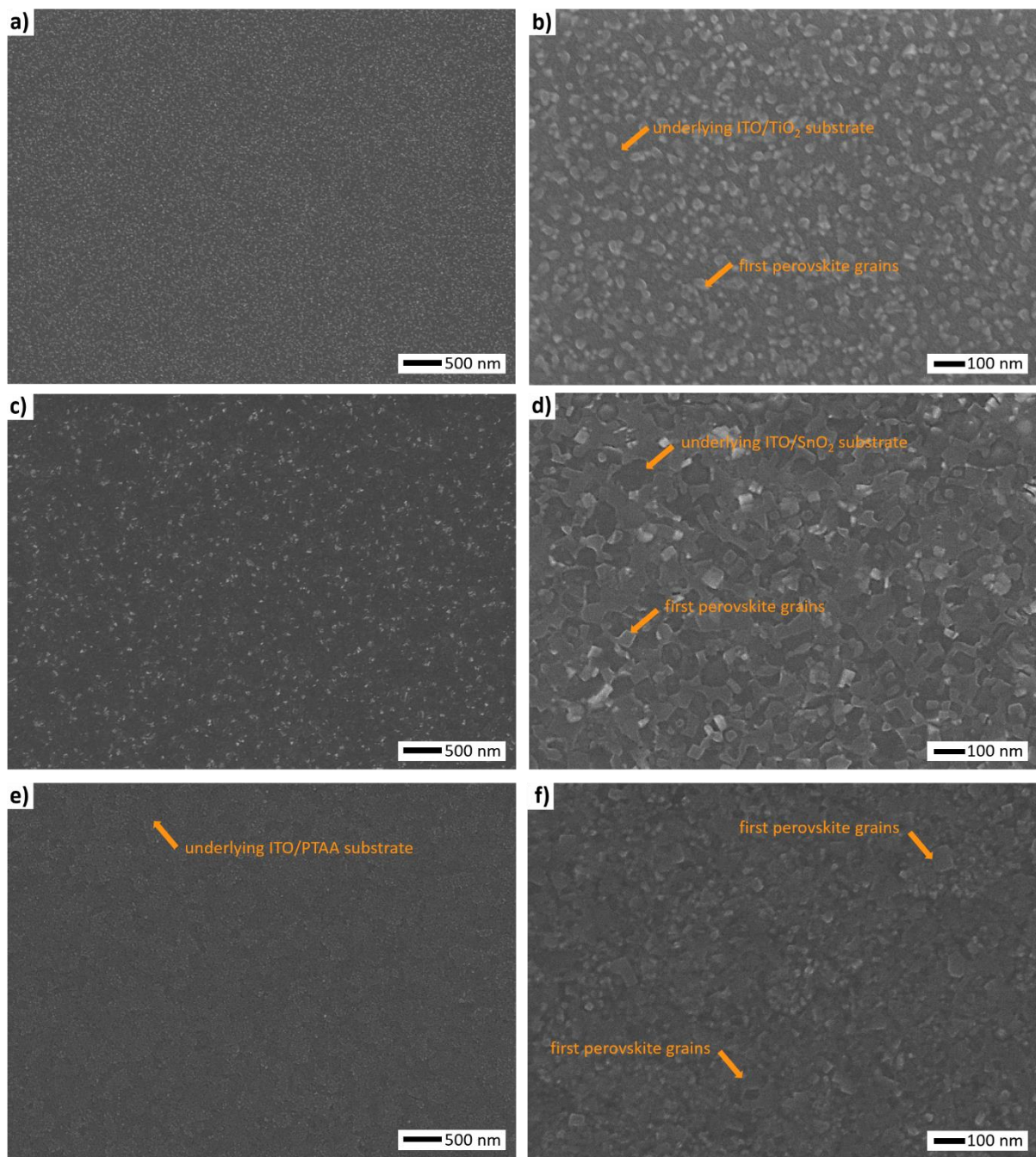
**Fig. S7.** SEM investigations of ultra-thin perovskite thin films (7 nm) deposited on top of (a-b) TiO$_2$, (c-d) SnO$_2$, and (e-f) PTAA. The left images show an area view, right images a zoom. On all substrates the formation of first perovskite grains can be observed. Initial grains are more pronounced on top of TiO$_2$ and especially SnO$_2$.
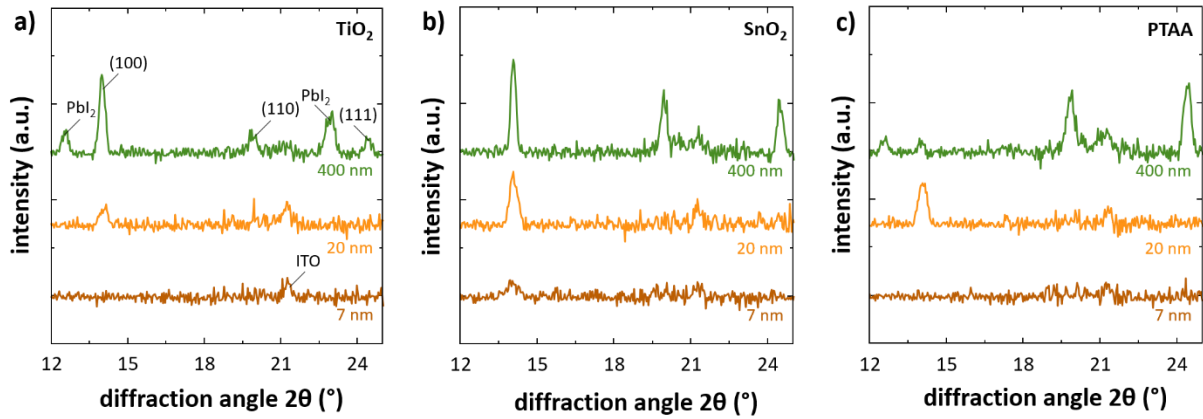
**Fig. S8.** High resolution X-ray diffraction (XRD) investigations on ultra-thin perovskite absorbers grown on top of (a) $TiO_2$, (b) $SnO_2$, and (c) PTAA. In agreement with the defined grain structure at the interface between absorber and substrate apparent from the cross-sectionals images (see Figure 4 in the main manuscript), no crystalline $PbI_2$ layer is identified for any of the substrate materials in the initial phase of grain formation. On the contrary, a first crystalline perovskite phase is already forming for the thinnest perovskite layer grown on $SnO_2$, illustrating the good detection limit also for ultra-thin crystalline layers. In agreement with the SEM studies from before, a delay in conversion of $PbI_2$ into perovskite in case of $TiO_2$ is observed only in a later stage (400 nm) of film formation while defined perovskite grains form in the beginning of film formation (20 nm).
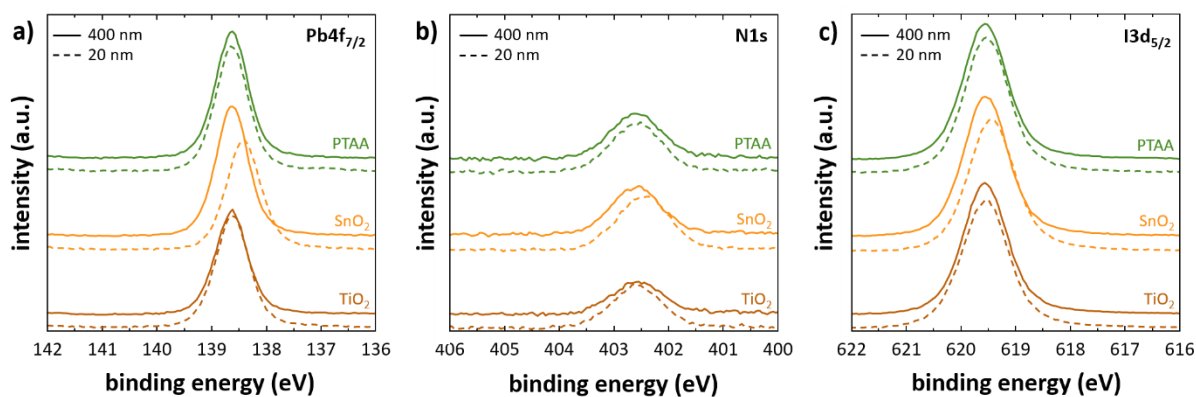
8

**Fig. S9.** X-ray photoelectron spectroscopy (XPS) investigations of thin (20 nm) and thick (400 nm) perovskite absorbers grown on top of $TiO_2$, $SnO_2$, and PTAA. Evaluated are the (a) Pb4f$_{7/2}$, (b) N1s, and (c) I3d$_{5/2}$ states. The spectra indicate a homogenous film formation with only minor changes in absorber composition throughout the course of film formation (see Table S1 below). All spectra of the thin perovskite thin films on top of $SnO_2$ are slightly shifted by $< 250$ meV to lower binding energies, which is most likely a p-type doping effect due to a slight excess of MAI. Strongest alterations in composition (especially in nitrogen content) during film formation are observed for absorbers grown on top of $TiO_2$.

| substrate | thickness (nm) | N (at.%) | Pb (at.%) | I (at.%) |
|-----------|----------------|----------|-----------|----------|
| TiO$_2$ | 20 | 16.8 | 19.3 | 64.0 |
| | 400 | 13.9 | 18.4 | 67.7 |
| SnO$_2$ | 20 | 20.4 | 18.0 | 61.6 |
| | 400 | 17.2 | 20.3 | 62.6 |
| PTAA | 20 | 18.2 | 19.9 | 62.0 |
| | 400 | 17.4 | 20.2 | 62.4 |

**Tab. S1.** Perovskite composition for thin (20 nm) and thick (400 nm) absorbers grown on top of different substrate materials as extracted from X-ray photoelectron spectroscopy (XPS) investigations (see Figure S8 above). A homogeneous composition during the deposition is especially achieved for absorbers grown on top of PTAA, which is in agreement to the distinct columnar grain growth for these absorbers. Absorbers grown on TiO$_2$ appear low in nitrogen content, which might be linked to the delayed conversion of PbI$_2$ into perovskite observed for absorbers grown on top of TiO$_2$.
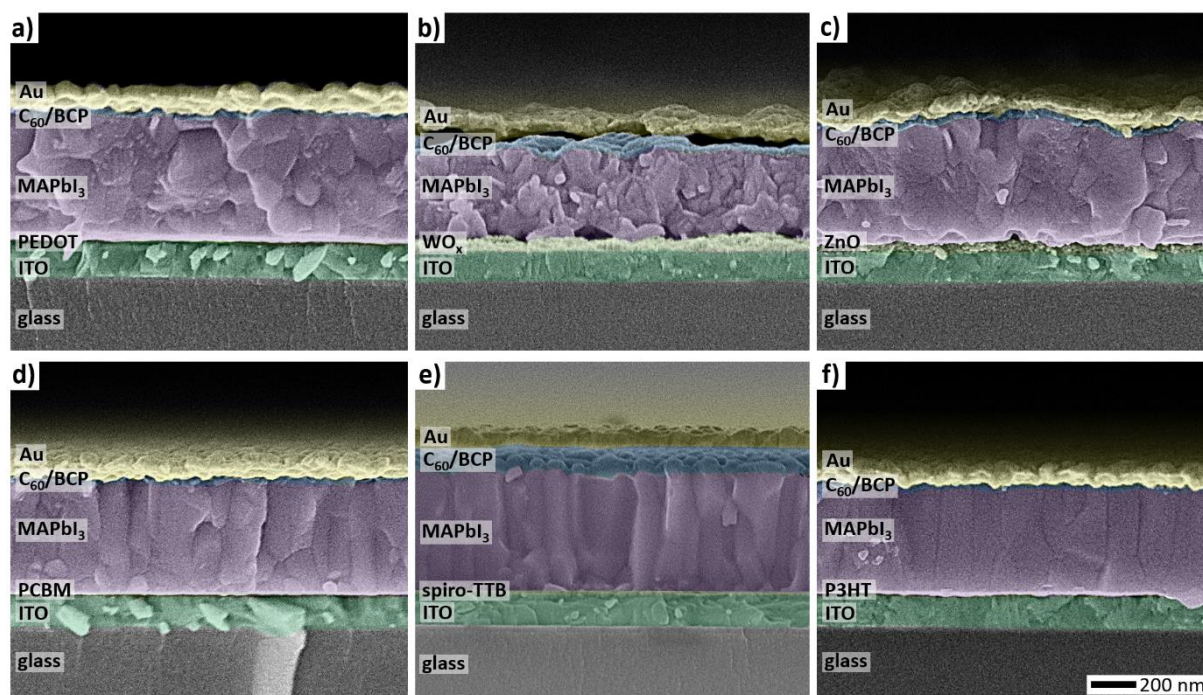
**Fig. S10.** Grain growth of co-evaporated perovskite absorbers grown on top of additional substrate materials in conjunction with those highlighted in the main manuscript. Shown are cross-sectional SEM images of perovskite absorbers grown on the alternative substrate materials (a) PEDOT:PSS, (b) $WO_x$, (c) ZnO, (d) PCBM, (e) spiro-TTB, and (f) P3HT. In agreement with the differences in grain orientation obtained from the XRD study (see Figure S6 above), a distinct columnar grain growth is only achieved for absorbers grown on P3HT and spiro-TTB (similar to the case of PTAA), while absorbers grown on top of PEDOT:PSS and ZnO exhibit small grains with various horizontal grain boundaries as well as the formation of phase segregations (similar to the case of $SnO_2$). Similar to the case of absorbers grown on top of $TiO_2$, absorbers grown on $WO_x$ form a highly disturbed absorber morphology with a less defined grain structure. Finally, PCBM cannot be classed as one of the clearer cases mentioned before but is rather a borderline case between $SnO_2$ and PTAA with well-defined grain structure, with smaller vertical grain size accompanied by horizontal grain boundaries, which is also in agreement with the classification between spiro-TTB and ZnO in the previous XRD study. All images have the same magnification. In order to improve the

quality of the cross-sectional images, all absorbers were equipped with a thin $C_{60}$ and Au layer on top of the absorber.
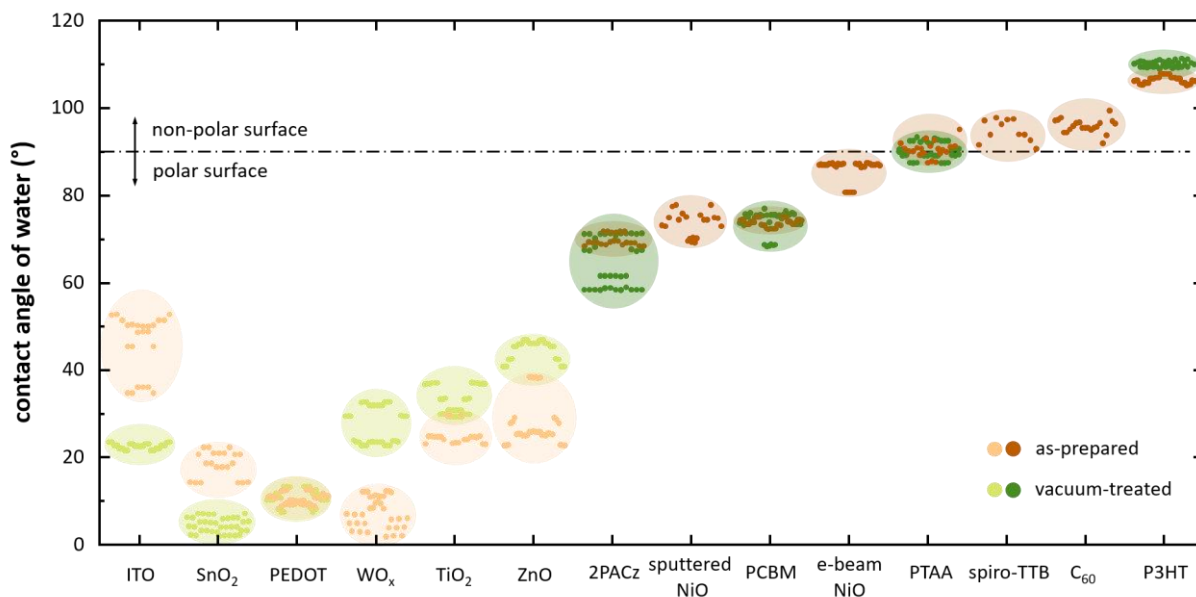
**Fig. S11.** Influence of a vacuum treatment on the surface polarity of commonly employed charge transport layers by water contact angle measurements. Slight differences are observed for some substrate materials, which are linked to a removal of residual solvents of the solution-based layers as well as water that might stick on top of the surface (e.g. for layers prepared under ambient conditions). However, the general trend in surface polarity of the different substrate materials is not significantly affected by a vacuum treatment. Nevertheless, values obtained from vacuum-treated substrates are used throughout this work since they describe a more realistic scenario for vacuum processed perovskite solar cells. All charge transport materials were deposited on top of an ITO front electrode. Vacuum treated substrates were kept in vacuum ($< 5\times10^{-7}$ mbar) overnight and immediately measured after venting the vacuum system. Charge transport layers fabricated by vacuum-based methods did not undergo this vacuum step. For every substrate material several individual measurements were performed.
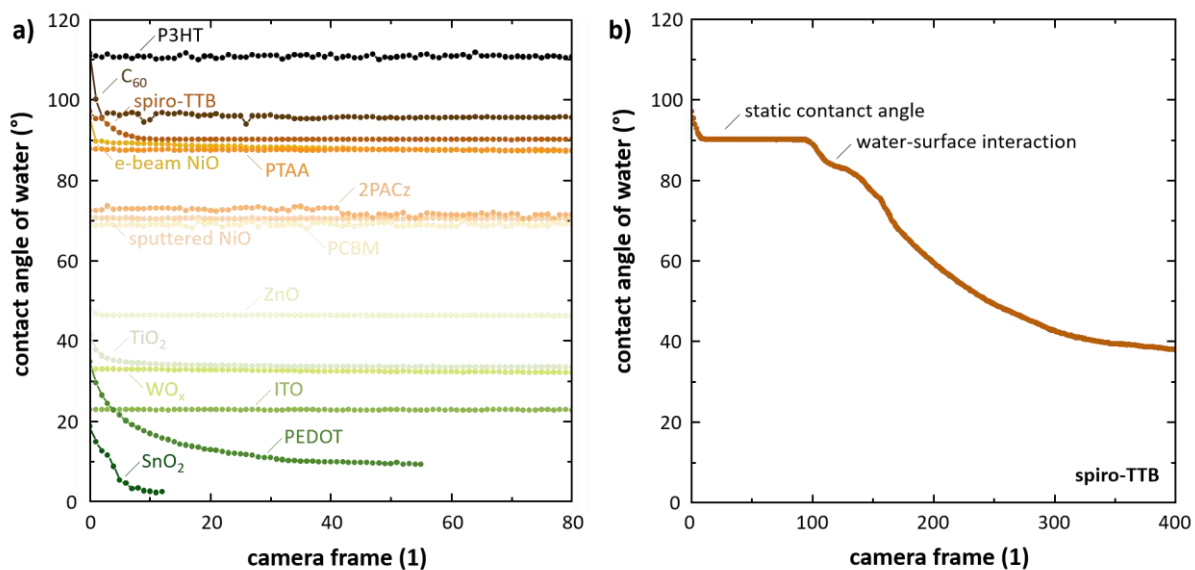
**Fig. S12.** Evolution of the water contact angle during the measurement. (a) Comparison of the temporal evolution of the contact angle for different substrate materials. Contact angles used for this work are static (constant) values, which were measured after a short settling time of the water droplet on the surface. Differences between static and non-static contact angles do not result in a change of the general trend between different substrate materials discussed in this work. (b) Long-term measurement of the contact angle for spiro-TTB. The use of a high-speed camera enables the measurement of the static contact angles before detrimental water-surface interactions set in (e.g. dissolving of the charge selective layer in water). All charge transport materials were deposited on top of an ITO front electrode and kept in vacuum (< $5\times10^{-7}$ mbar) overnight if not fabricated by vacuum-based methods. The measurement was performed with a frame rate of 45 fps.
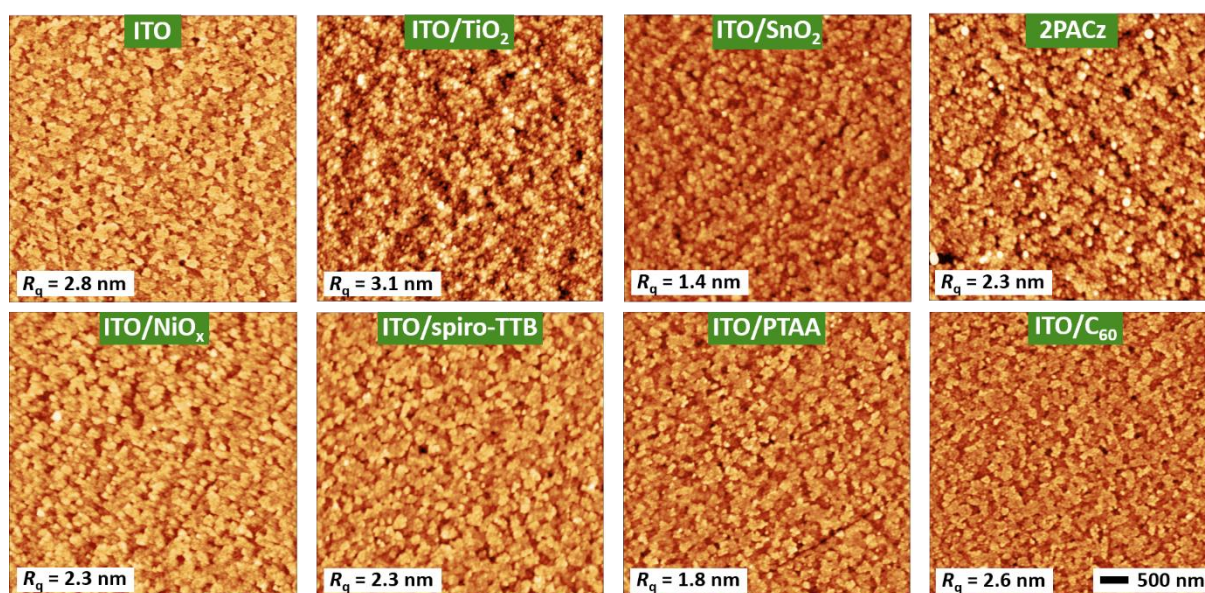
**Fig. S13.** Atomic force microscopy (AFM) surface investigation of a selection of different substrate materials employed in this study. The root mean square (RMS) roughness $R_q$ is below 5 nm for all substrate materials. Minor differences are observed for substrates employing $TiO_2$ with a slightly increased roughness as well as a lower retention of the ITO front electrode surface texture. All images have the same magnification.
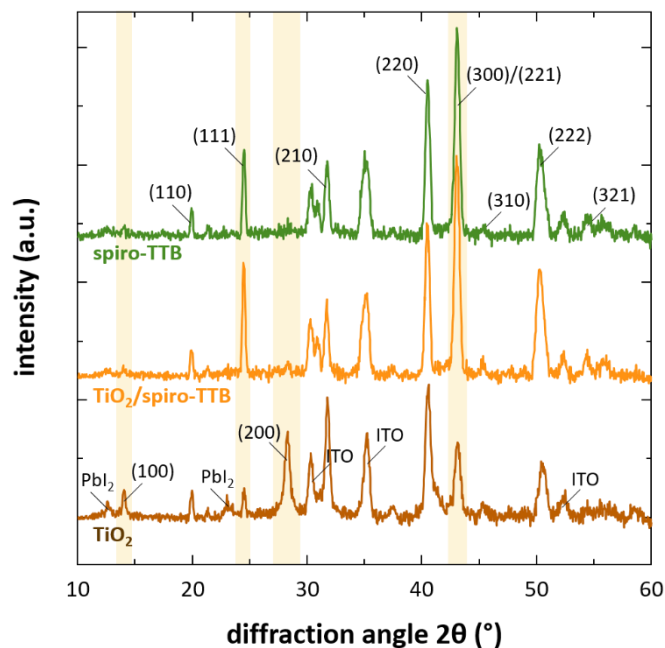
**Fig. S14.** Surface modification of the polar $TiO_2$ surface by a vacuum deposited non-polar spiro-TTB coating. In agreement with the previous discussions, the XRD pattern of the co-evaporated perovskite thin film on $TiO_2$ shows a delayed chemical conversion as indicated by the $PbI_2$ residuals present in these thin films as well as strong diffraction peaks related to the {100} crystal planes. Depositing a 2.5 nm thin conformal non-polar layer of spiro-TTB on top of the $TiO_2$ results in both an improved conversion of $PbI_2$ into perovskite together with a switching of the preferred crystal orientation (e.g. as indicated by the change in the (111)/(100) ratio) – similar to the behavior of the deposition for example on top of PTAA. The latter indicates that the dominant origin of the differences in growth dynamics is indeed the polarity of the substrate surface rather than its roughness. Deposition of the perovskite thin film on top of only spiro-TTB follows an identical trend as the $TiO_2$/spiro-TTB double layer. All samples were prepared in the same co-evaporation process and employ an ITO front electrode.
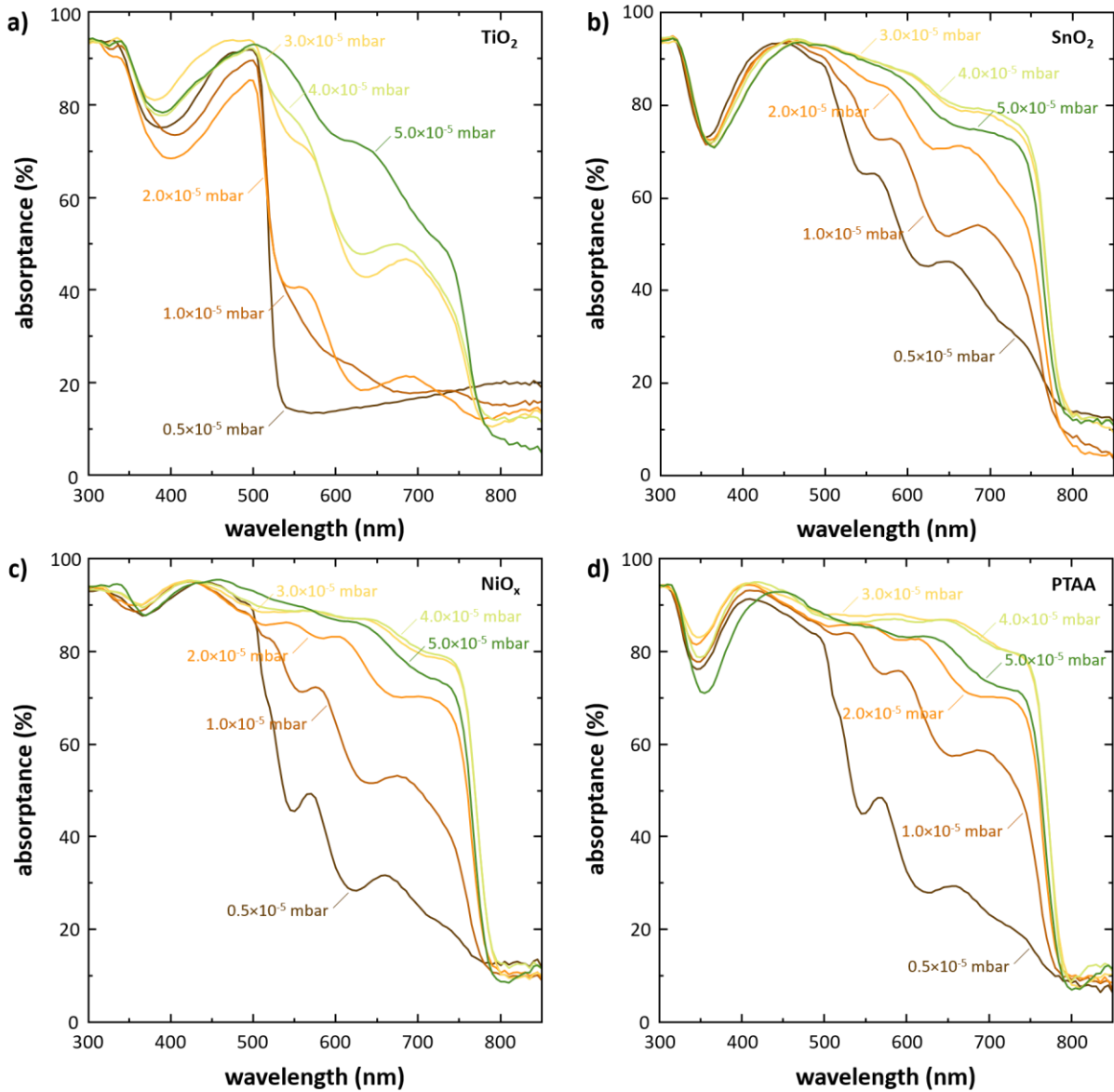
16

**Fig. S15.** Light absorptance for perovskite absorbers grown on various substrate materials at different MAI partial pressures. Shown are co-evaporated perovskite absorbers grown on (a) $TiO_2$, (b) $SnO_2$, (c) $NiO_x$, and (d) PTAA. In agreement with the trends in short-circuit current density an improved conversion of $PbI_2$ into perovskite is achieved by increasing the MAI partial pressure for all investigated substrate materials. However, differences in the effectivity of the incorporation of MAI into the $PbI_2$ matrix are obvious. A clear delay in conversion is observed for absorbers grown on top of $TiO_2$ while absorbers grown on top of $SnO_2$ indicate the most efficient conversion. Highest overall absorptance at ideal growth conditions is

achieved for absorbers grown on top of PTAA, which is consistent with the highest $J_{sc}$ values achieved for solar cells employing PTAA as substrate material. For all completely converted absorbers a drop in absorptance, and in turn also $J_{sc}$, is observed for the highest MAI partial pressures, which is explained either by a drop in effective absorber thickness due to the continuously decreasing mean free path at higher MAI partial pressures (see Figure 1 in the main manuscript) or a detrimental effect of excess MAI on the charge generation. Absorptance is calculated from the individual transmittance and reflectance measurements. Illumination was carried out from the substrate side.
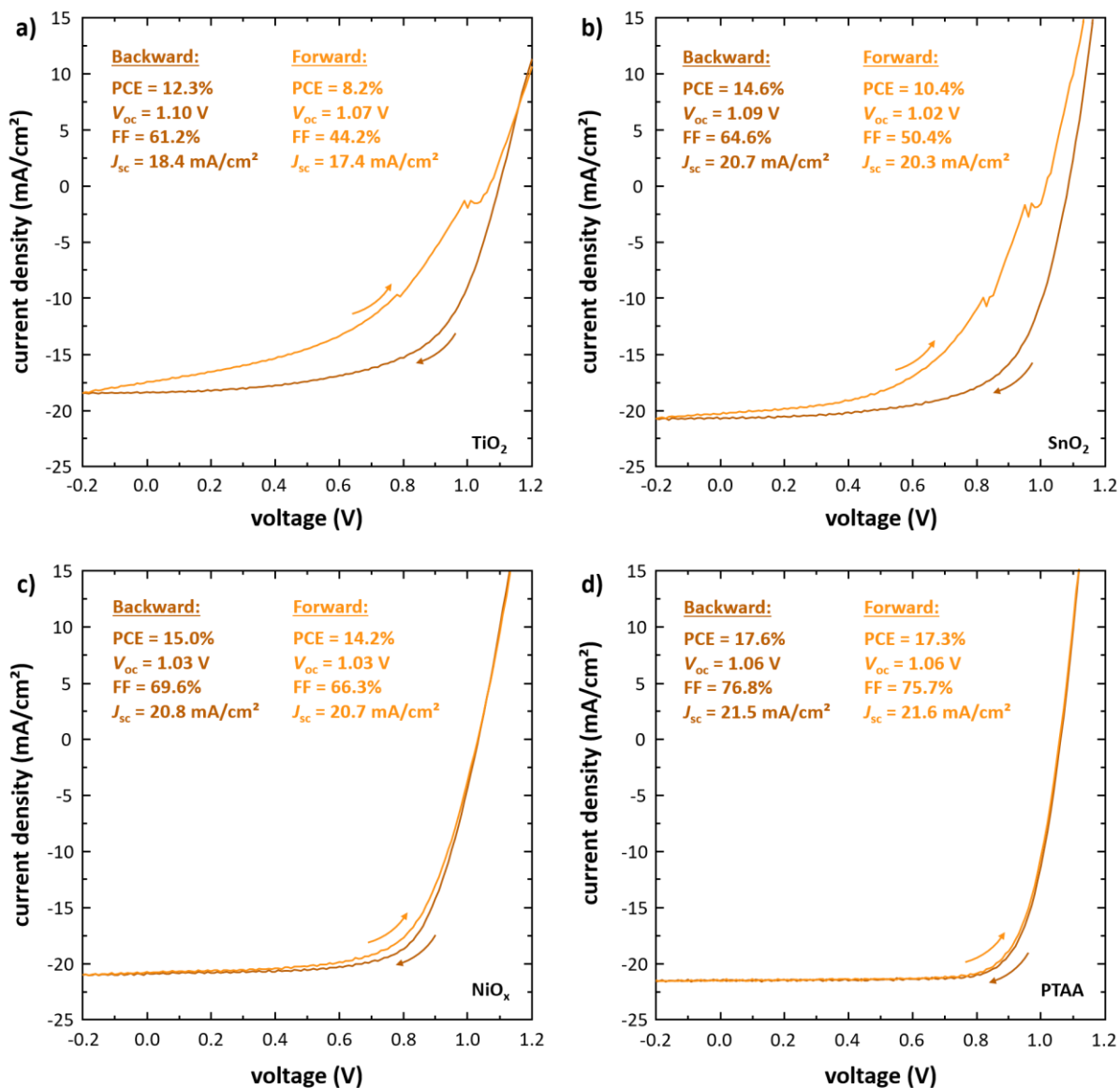
**Fig. S16.** *J-V*-characteristics of the best solar cells on different substrate materials fabricated in this study. Shown are solar cells based on co-evaporated perovskite absorbers grown on (a) $TiO_2$, (b) $SnO_2$, (c) $NiO_x$, and (d) PTAA. Clear differences are apparent in both performance and hysteresis of the different solar cells. In agreement with previous discussions, best performance is achieved for absorbers grown on PTAA. Best absorbers on different substrate material are deposited at different MAI partial pressures.
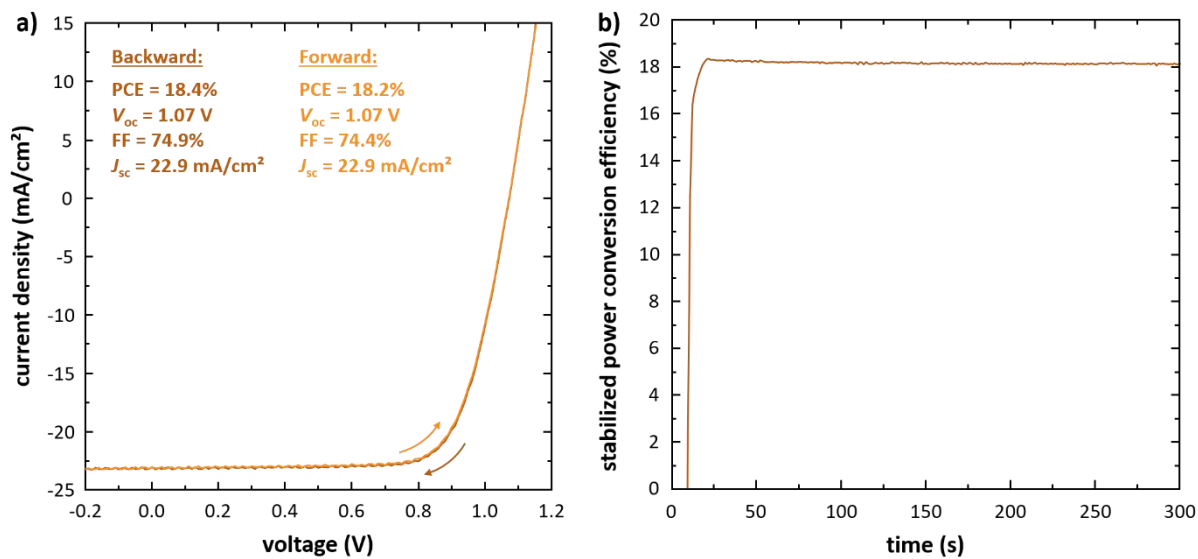
**Fig. S17.** Best solar cell with co-evaporated perovskite absorber grown on PTAA fabricated in this study. (a) *J-V*-characteristic in backward and forward direction. (b) Stabilized power output during MPP tracking under continuous illumination.
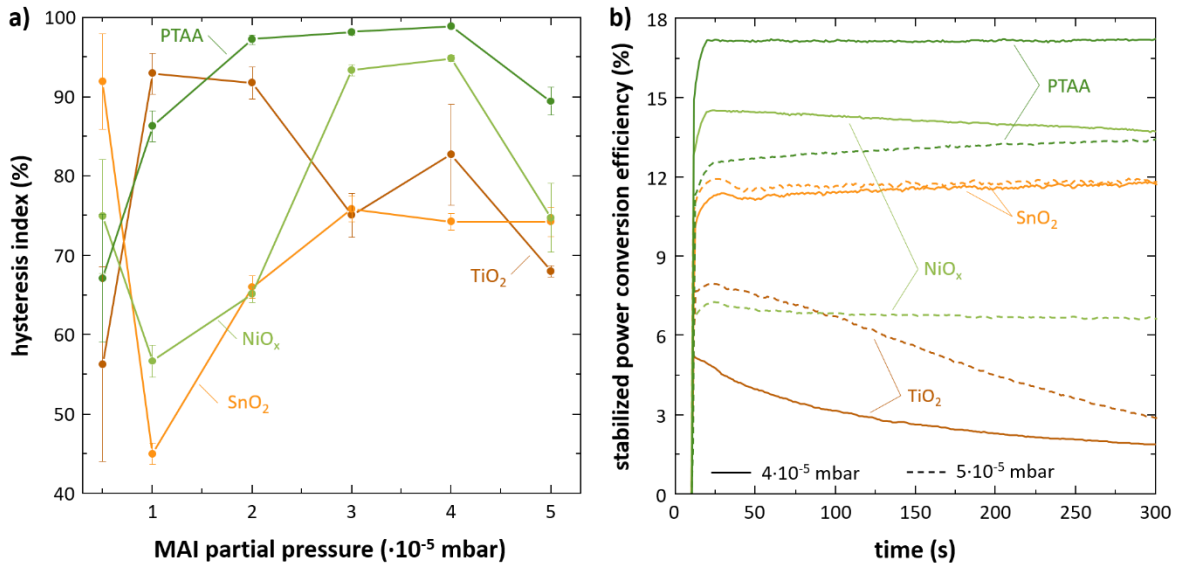
**Fig. S18.** Dependence of device stability on MAI partial pressure for perovskite solar cells employing different substrate materials. (a) Strong hysteresis is observed for absorbers grown on $SnO_2$ and especially $TiO_2$, while absorbers grown on $NiO_x$ and PTAA show negligible hysteresis in certain process windows. Similar to the trend in the solar cell parameters, the process window for PTAA is much wider than for $NiO_x$. The hysteresis index is calculated from ratio of the power conversion efficiency extracted from the backward and forward *J-V*-scan. (b) Stabilized power conversion efficiency (PCE) of solar cells prepared with different MAI partial pressures under continuous illumination for 5 min under MPP conditions. In agreement with previous investigations, best performance is achieved for solar cells employing PTAA as a substrate material. Perovskite absorbers grown on $NiO_x$ and more notably on $TiO_2$ exhibit severe stability problems, while the PCE absorbers grown on $SnO_2$ stabilize on these time scales, however, due to the strong hysteresis below the values achieved in the *J-V*-scans.
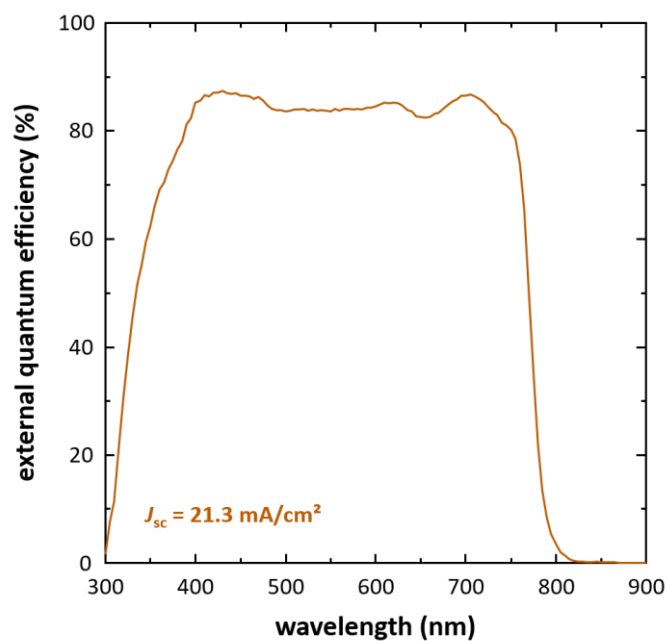
21

**Fig. S19.** External quantum efficiency (EQE) measurement performed on the champion solar cell in the all-evaporated layer stack sequence (see Figure 8 in the main manuscript). As a result of the low hysteresis in the devices, the short-circuit current density value extracted from EQE is in good agreement with the value obtained from the *J-V*-scan.
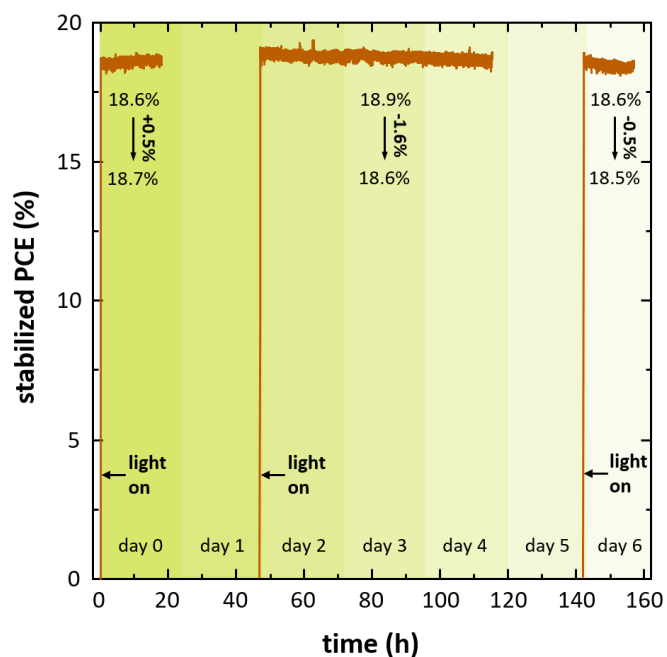
**Fig. S20.** Measurement of the stabilized power output performed on the champion solar cell in the all-evaporated layer stack sequence for several hours (see also Figure 8 in the main manuscript). During measurement, the maximum power point was continuously tracked. The measurement was carried under continuous AM1.5g illumination in inert atmosphere. Temperature of the device was kept at 25 °C. Between the measurements, the samples were stored in dark in inert atmosphere.
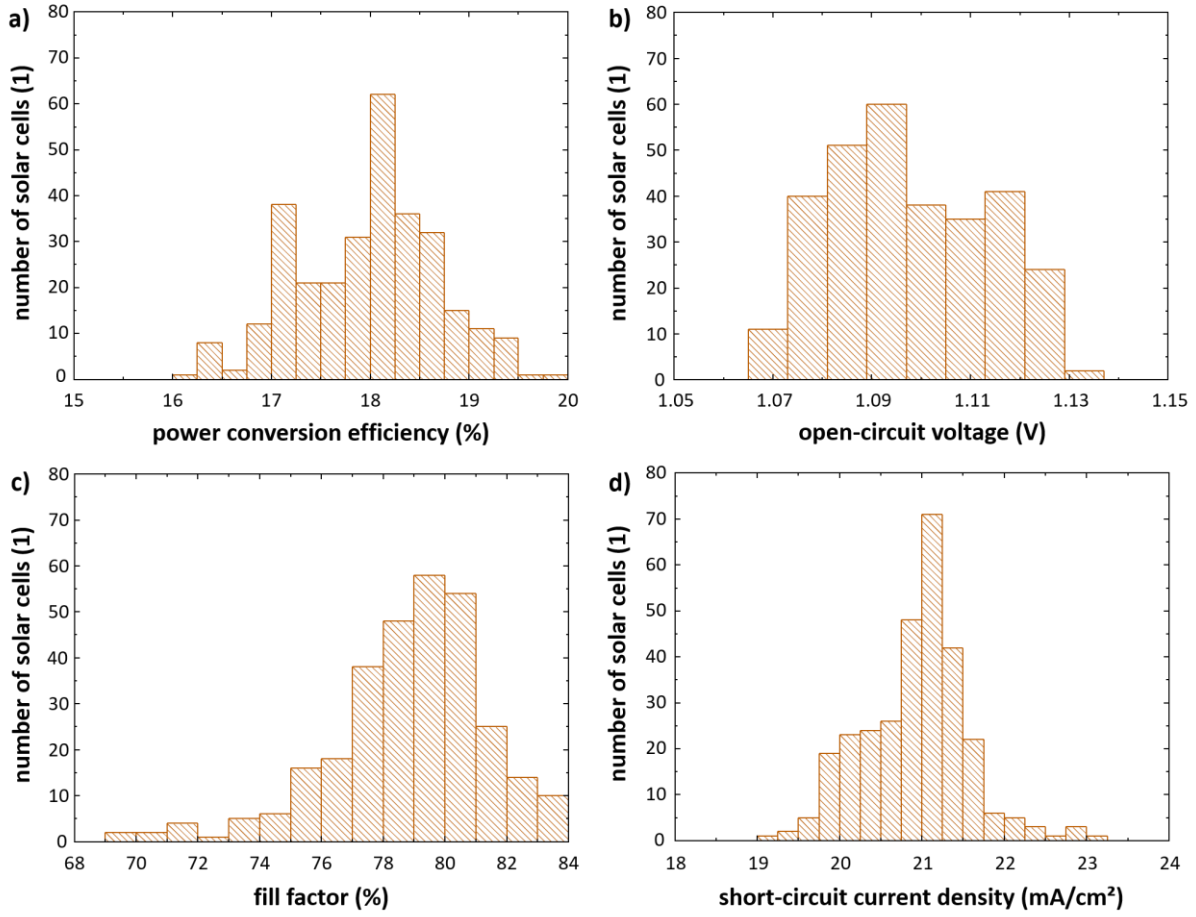
**Fig. S21.** Statistical distribution of solar cell parameters for co-evaporated solar cells employing spiro-TTB as substrate material. The total number of investigated solar cells, fabricated in 24 consecutive evaporation runs, is 302. Shown are the distributions of (a) the power conversion efficiency (PCE), (b) the open-circuit voltage ($V_{oc}$), (c) the fill factor (FF), and (d) the short-circuit current density ($J_{sc}$). Variations in these parameters arise from slight variations in perovskite composition and absorber thickness.